JOURNAL OF MAGNETIC RESONANCE **130,** 86–96 (1998)
ARTICLE NO. MN971285

Nutation-Frequency Correlated EPR Spectroscopy: The PEANUT Experiment

S. Stoll, G. Jeschke,[1] M. Willer, and A. Schweiger

Laboratorium für Physikalische Chemie, Eidgenössische Technische Hochschule, 8092 Zürich, Switzerland

Received May 9, 1997

The phase-inverted echo-amplitude detected nutation (PEANUT) experiment for the measurement of transient electron spin nutation frequencies is introduced. In this new pulse sequence, nutation refocused to a rotary echo is detected via the amplitude modulation of a primary electron spin echo. Since detection and excitation of the nutation are fully separated in time, experiments at very high nutation frequencies become feasible. The nutation frequencies which are proportional to the transition moment of an EPR transition can be used to label individual EPR lines by an additional parameter. Using a two-dimensional PEANUT experiment which correlates the nutation frequencies with the resonance fields, the interpretation of complicated field-swept EPR spectra can considerably be simplified. A theoretical description of the experiment is given and the inner working of the approach is described. The predicted features of PEANUT spectra are verified experimentally and examples of applications to both ordered and disordered systems are given.

Key Words: **electron spin resonance; pulse EPR; transient nutation; 2D EPR; transition moments.**

INTRODUCTION

In solid-state EPR spectra the transition frequencies depend on the anisotropic magnetic interactions characterizing the spin system and on the orientation of the paramagnetic species with respect to the external magnetic field vector. In many cases, particularly in orientationally disordered systems, it is difficult or even impossible to extract all the magnetic parameters from a conventional field-swept continuous wave (CW) EPR spectrum. Pulse methods offer various possibilities for *labeling* an EPR transition by an additional parameter that depends, for example, on the change of the resonance frequency of a line upon reorientation (anisotropy-resolved EPR (*1*)), or on the g value of a particular transition (electron Zeeman-resolved EPR (*2*)). In a two-dimensional (2D) plot representing the signal intensity as a function of both the B_0 field and this additional parameter, the disentangled EPR spectrum is then much easier to interpret.

Another parameter for labeling individual EPR transitions is the transition moment, which is in general different for different transitions. A recently introduced approach that makes use of the transition moments to spread an EPR spectrum into a second dimension is forbidden-transition-labeled EPR (FORTE) (*3*). FORTE is based on a hole-burning experiment and allows the separation of allowed and forbidden EPR transitions. Another scheme makes use of the proportionality between the transition moment and the frequency at which an electron or nuclear spin ensemble nutates under microwave (MW) or radio frequency irradiation (*4, 5*). In NMR and NQR spectroscopy, transient nutation experiments are frequently used to elucidate quadrupolar interactions of nuclei with half-integer spin (*6*), whereas in pulse electron nuclear double resonance, where the nutation of the nuclear spins is indirectly observed via the electron spin, the approach can be used to determine the number of equivalent nuclei (*7*).

In EPR, 1D and 2D transient nutation techniques have been applied to investigate excited triplet states and spin-correlated radical pairs (*8–12*), to determine electron spin multiplicities (*13–16*), to discriminate between allowed and forbidden transitions (*15*), and to separate overlapping EPR spectra (*15*). In these electron spin nutation experiments, the signal is recorded either directly during MW irradiation or after MW irradiation by measuring a free induction decay or a primary electron spin echo.

In this work we introduce the *p*hase-inverted *e*cho-*a*mplitude detected *nut*ation (PEANUT) experiment (*17*) which is based on the measurement of an electron-spin-echo-detected rotary echo (*18*). In the proposed pulse scheme shown in Fig. 1, MW irradiation and signal detection are separated in time, and nutation frequency distributions are partly refocused. Compared to the known nutation schemes used in EPR spectroscopy, PEANUT is distinguished by a number of advantages.

— *Direct detection:* The detection of the transient nutation signal *during* MW irradiation (*8, 11, 15*) suffers from low nutation frequencies, since at higher MW power leakage

[1] Current address: Universität Bonn, Institut für Anorganische Chemie, D-53121 Bonn, Germany.

1090-7807/98 $25.00

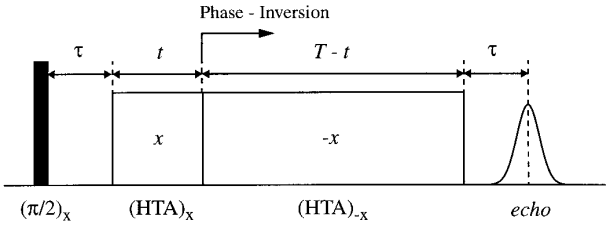

FIG. 1. Pulse sequence for the PEANUT experiment. The HTA pulse that nutates the spins is subdivided into two parts which differ in phase by π and create a rotary echo at $t = T/2$.

fed to the detection system makes the measurement of the nutation signal impossible.

—*FID detection:* Nutation can also be detected by monitoring the amplitude of the FID that follows a high-turning-angle (HTA) pulse, as a function of pulse duration T. Fourier transformation of the FID yields the EPR spectrum with peak amplitudes oscillating with time T (*13, 14, 16*). In a 2D representation the resonance frequencies are then again correlated with the nutation frequencies (*10*). This scheme works well for EPR spectra with a small frequency range and narrow lines. However, for broad spectra it is no longer possible to excite all the transitions and for the limiting case $\Gamma_{\text{inh}} \gg \omega_1$, the FID changes its character completely: a so-called oscillatory FID of length T is observed with frequencies that are no longer related to the resonance offsets of particular EPR lines (*19*).

—*Echo detection:* The magnetization of the nutating spins can also be observed by using echo detection. Two such schemes have been proposed. In the first experiment, the transverse magnetization that dephases during time τ after a single HTA pulse is refocused by a π pulse to an echo observed at 2τ (*16*). In the second experiment, the two-pulse sequence $\pi/2-\tau-\pi-\tau-$echo applied at time t after the HTA pulse detects the longitudinal magnetization present at the end of the HTA pulse (*9*). In the latter scheme time t is long compared to T_2 but short compared to T_1, so that all the electron coherence has decayed. In both echo methods the length of the HTA pulse is incremented. However, in these schemes the B_1-field inhomogeneity is not refocused.

The advantages of the PEANUT experiment presented in this work can be summarized as follows: High nutation frequencies can be generated and observed; B_1-field inhomogeneities are refocused; the frequency window of spins that contribute to the signal is controlled by the preparation pulse; there is no relaxational broadening; intensities of forbidden transitions can be increased by using preparation pulses with effective $\pi/2$ flip angles; undesired peaks caused by nuclear spins are weak; the data also contain the field-swept EPR spectrum (spin-lock projection).

First, we briefly review the dependence of the transition moment of an EPR transition on the various magnetic parameters. Then we give a rigorous theoretical treatment of the PEANUT experiment based on the density operator formalism and discuss the inner working of the scheme. Finally, we verify experimentally the features predicted by theory and demonstrate the potential of the method by two examples of application.

NUTATION FREQUENCIES

An electron–nuclear spin system with an effective electron spin S and n nuclear spins I in the presence of MW irradiation is described in the laboratory frame by the spin Hamiltonian (in angular frequency units)

$$H = H_0 + H_1, \qquad [1]$$

with the static Hamiltonian

$$\begin{aligned} H_0 &= H_{\text{EZ}} + H_{\text{ZFS}} + H_{\text{HFS}} + H_{\text{NQ}} + H_{\text{NZ}} \\ &= \beta_e \mathbf{B}_0 \mathbf{g} \mathbf{S}/\hbar + \mathbf{S}\mathbf{D}\mathbf{S} \\ &\quad + \sum_{i=1}^{n} (\mathbf{S}\mathbf{A}_i I_i + I_i \mathbf{Q}_i I_i - \beta_n g_{ni} \mathbf{B}_0 I_i/\hbar) \end{aligned} \qquad [2]$$

and the perturbation

$$H_1 = \beta_e 2\mathbf{B}_1 \mathbf{g} \mathbf{S}/\hbar. \qquad [3]$$

$\mathbf{B}_0$ is the static magnetic field vector along the z axis and $2\mathbf{B}_1 = 2B_1 \cos(\omega_{\text{MW}} t)\mathbf{e}_x$ is the linearly polarized MW field chosen along x with frequency ω_{MW} and amplitude $2B_1$. The observed signal, and in particular its nutation frequency ω_{TN} are complicated functions of the quantities $\mathbf{g}$, $\mathbf{D}$, $\mathbf{A}_i$, and $\mathbf{Q}_i$, the vectors $\mathbf{B}_0$ and $\mathbf{B}_1$, the resonance offset, and the changes of the magnetic quantum numbers Δm_S and Δm_I^i that characterize a particular transition. To follow the time evolution of the spin system, one must solve the Liouville–von Neumann equation

$$\dot{\sigma}(t) = -i[H, \sigma(t)], \qquad [4]$$

which is usually done in a rotating frame where H is time-independent. The observed signal is then proportional to the trace of the product of the matrix representation of $\sigma(t)$ and the detection operator. In the following we briefly discuss the nutation of electron spins for some special systems.

$S = \frac{1}{2}$, *isotropic* $\mathbf{g}$. This two-level system which represents the most simple situations is described by the rotating frame Hamiltonian

$$H = \Omega_S S_z + \omega_1 S_x, \qquad [5]$$

with the pumping field along x, the resonance offset $\Omega_S = \beta_e g\mathbf{B}_0/\hbar - \omega_{MW}$ and the MW field strength in angular frequency units $\omega_1 = \beta_e g\mathbf{B}_1/\hbar$ (note that these expressions contain the g value which is spin-system specific). Starting from thermal equilibrium and assuming $\omega_1 \gg 1/T_2 \gg 1/T_1$ for the longitudinal relaxation time T_1 and the spin–spin relaxation time T_2 (extreme underdamping), the signal along y for a particular off-resonance spin packet is given by (*8*)

$$S_y(t) \propto \frac{\omega_1}{\omega_{TN}} \sin(\omega_{TN}t)\exp\left[-\frac{t}{T_2}\left(1 - \frac{1}{2}\frac{\omega_1^2}{\omega_{TN}^2}\right)\right], \quad [6]$$

with the nutation frequency

$$\omega_{TN} = [\omega_1^2 + \Omega_S^2]^{1/2}. \quad [7]$$

A similar expression is found for $S_x(t)$. The angle θ between the nutation axis ω_{TN} and the z axis is defined by

$$\tan\theta = \omega_1/\Omega_S. \quad [8]$$

For an inhomogeneous line of width $\Gamma_{inh} \gg \omega_1$ excited at the center, the integrated signal (excluding times $t < 1/\omega_{TN}$) is given by

$$S_y(t) \propto \omega_1 f(\omega_{MW}) J_0(\omega_1 t)\exp(-t/2T_2), \quad [9]$$

where $f(\omega_{MW})$ is the value of the normalized lineshape function at the center of the line and $J_0(\omega_1 t)$ is the zeroth-order Bessel function of the first kind, which describes an additional damping. $S_x(t)$ vanishes, since it contains only terms that are odd with respect to Ω_S.

$S = \frac{1}{2}$, anisotropic $\mathbf{g}$. The situation with an anisotropic $\mathbf{g}$ matrix is much more complicated (*20*). For an axially symmetric $\mathbf{g}$ matrix Eq. [9] takes the form

$$S_y(t) \propto \omega_1^{eff} f(\omega_{MW}) J_0(\omega_1^{eff} t)\exp(-t/2T_2), \quad [10]$$

with

$$\omega_1^{eff} = \beta_e B_1 g_1/\hbar \quad [11]$$

$$g_1 = (g_\perp/g)\,(g^2\sin^2\alpha + g_\parallel^2\cos^2\alpha)^{1/2} \quad [12]$$

$$g = (g_\parallel^2\cos^2\beta + g_\perp^2\sin^2\beta)^{1/2}, \quad [13]$$

and the Euler angles α, β (*21*). This dependence of the nutation frequency ω_1^{eff} on the $\mathbf{g}$ matrix can be used to separate overlapping EPR spectra of different species or different sites in single crystals (*15*). Since the nutation frequency is related to the g value along $\mathbf{B}_1$, the approach can also be used to determine g values that are not accessible in a field-swept EPR experiment. In particular it has been demonstrated that extremely small g values corresponding to resonance fields B_0 far beyond the available range can *indirectly* be measured via the nutation frequency (*20*).

$S = \frac{1}{2}$, $I = \frac{1}{2}$, isotropic $\mathbf{g}$. For this simple two-spin system the rotating frame frequencies of the two allowed and two forbidden transitions are given by

$$\omega_a = \Omega_S \pm \tfrac{1}{2}(\omega_\alpha - \omega_\beta) \quad [14]$$

and

$$\omega_f = \Omega_S \pm \tfrac{1}{2}(\omega_\alpha + \omega_\beta), \quad [15]$$

with

$$\left|\begin{matrix}\omega_\alpha \\ \omega_\beta\end{matrix}\right| = \left[\left((\omega_I \pm \frac{A}{2}\right)^2 + \left(\frac{B}{2}\right)^2\right]^{1/2}, \quad [16]$$

$A = A_{zz}$, $B = (A_{zx}^2 + A_{zy}^2)^{1/2}$, and the nuclear Zeeman frequency $\omega_I = -\beta_n g_n B_0/\hbar$. For the corresponding on-resonance nutation frequencies we find

$$\omega_{TN}^{a} = \left(\frac{|\omega_I^2 - \tfrac{1}{4}(\omega_\alpha - \omega_\beta)^2|}{\omega_\alpha\omega_\beta}\right)^{1/2}\omega_1 = I_a^{1/2}\omega_1 \quad [17]$$

$$\omega_{TN}^{f} = \left(\frac{|\omega_I^2 - \tfrac{1}{4}(\omega_\alpha + \omega_\beta)^2|}{\omega_\alpha\omega_\beta}\right)^{1/2}\omega_1 = I_f^{1/2}\omega_1, \quad [18]$$

where I_a and I_f are the transition probabilities of the allowed and forbidden transitions, respectively (*22*). Since in most cases $I_a \gg I_f$, the nutation experiment can be used to separate allowed and forbidden transitions (*15*).

$S > \frac{1}{2}$, isotropic $\mathbf{g}$. The investigation of spin systems with $S > \frac{1}{2}$ is complex for $|H_{ZFS}| \approx |H_1|$. Note that this is analogous to quadrupole nutation in NMR (*23*) and that the theoretical results for $I = \frac{3}{2}$ (*23–25*) and $I = \frac{5}{2}$ (*24–26*) systems can also be applied to the EPR case. For $|H_{ZFS}| \ll |H_1|$, the on-resonance nutation frequency ω_{TN} is simply given by ω_1, whereas for $|H_{ZFS}| \gg |H_1|$ and a transition $|S, m_S'\rangle \leftrightarrow |S, m_S\rangle$, it is described by

$$\omega_{TN} = [S(S+1) - m_S m_S']^{1/2}\omega_1. \quad [19]$$

In the latter case the nutation experiment can therefore be used to determine the electron spin quantum number S and to identify the various electron spin transitions (*13–16*).

THE PEANUT EXPERIMENT

The pulse sequence for the PEANUT experiment shown in Fig. 1 is basically a two-pulse primary spin echo sequence with the refocusing π pulse replaced by a special composite nutation pulse. First, an MW $\pi/2$ pulse is applied whose length determines the frequency window of the spins involved in the experiment. The transverse magnetization excited by this pulse evolves and dephases during the first free evolution period of length τ. Then an HTA pulse of constant length T is applied. However, in contrast to the locked-echo sequence (*27*) the HTA pulse in PEANUT is subdivided into two parts of variable length t and $T - t$ with opposite MW phases 0 and π.

During time t the MW field is applied along the x axis, so that the magnetization vector of an individual spin packet with resonance offset Ω_S nutates with frequency ω_{TN} around an effective field axis $\boldsymbol{\omega}_{TN}$ in the xz plane that deviates from the z axis by the angle θ. During time $T - t$ the MW field is applied along the $-x$ axis, and the spin packet now nutates with the same frequency ω_{TN} around the corresponding effective field axis $\boldsymbol{\omega}_{TN}$ in the $-xz$ plane. The phase shift at time t causes a partial refocusing of both the off-resonance contributions and the inhomogeneity of the B_1 field; the refocusing is optimum for $t = T - t = T/2$. Note that the formation of a rotary echo in the PEANUT experiment is more complex than in a conventional rotary echo experiment (*18*), where the spin system is in thermal equilibrium before the HTA pulse is applied. After the HTA pulse the spins again freely evolve and form a primary echo at time τ. As an alternative to the proposed PEANUT experiment one could think of a sequence with an HTA pulse without phase change and variable length T. However, this simpler scheme suffers from the disadvantage of having a ''deadtime'' for short T values of up to 40 ns. Experiments corroborate that PEANUT is by far superior to such a simplified approach.

The motion of the magnetizations of the individual spin packets during this pulse sequence is quite complicated, so that a visualization in terms of magnetization trajectories on a unit sphere does not provide much insight. In a 2D PEANUT experiment, the echo amplitude is recorded as a function of time t, which is varied between 0 and T, and the magnetic field strength B_0. Since the total length of the sequence is kept constant during the experiment, the influence of relaxation processes on the echo intensity is the same during the entire data acquisition.

An analytical formula for the PEANUT sequence has been derived for an isotropic $S = \frac{1}{2}$ electron spin system (*17, 28*) by using SOME (*29*), a Mathematica package for carrying out symbolic product operator manipulations. An inhomogeneously broadened symmetric EPR line excited at the center is assumed, so that terms that are odd functions with respect to Ω_S can be skipped; relaxation is neglected. A selective preparation pulse along x of length t_p, field strength ω_p and nominal flip angle $\omega_p t_p = \pi/2$, and the two-step phase cycle $[0, 0, \pi] - [\pi, 0, \pi]$ to eliminate the oscillatory FID that results from polarization present after this preparation pulse are used. Under these assumptions, the signal of an individual spin packet with resonance offset Ω_S along y at time τ after the HTA pulse is given by (*28*)

$$S_y(t) \propto c_0 + c_{2c}\cos\left(2\omega_{TN}\left(t - \frac{T}{2}\right)\right) + c_{2s}\sin\left(2\omega_{TN}\left(t - \frac{T}{2}\right)\right) + c_{1c}\cos(\omega_{\mathrm{TN}}t) + c_{1s}\sin(\omega_{\mathrm{TN}}t), \quad [20]$$

with a constant term c_0, the coefficients

$$\begin{aligned}
c_{2c} &= \sin^2\theta \sin\zeta \{\sin(\omega_{\mathrm{eff}}t_p)[1 - \sin^2\theta \sin^2(\Omega_S\tau)] \\
&\quad + (\cos(\omega_{\mathrm{eff}}t_p) - 1)\sin^2\theta \cos\zeta \\
&\quad \times \sin(\Omega_S\tau)\cos(\Omega_S\tau)\}, \\
c_{2s} &= \sin^2\theta \sin\zeta \cos\theta \cos\zeta(\cos(\omega_{\mathrm{eff}}t_p) - 1), \\
c_{1c} &= -2\cos\theta \sin^2\theta \sin\zeta \{\cos(\Omega_S\tau)\sin(\omega_{\mathrm{TN}}T) \\
&\quad + \sin(\Omega_S\tau)\cos\theta[1 + \cos(\omega_{\mathrm{TN}}T)]\} \\
&\quad \times \{\sin(\omega_{\mathrm{eff}}t_p)\sin(\Omega_S\tau) - (\cos(\omega_{\mathrm{eff}}t_p) - 1) \\
&\quad \times \cos\zeta \cos(\Omega_S\tau)\}, \\
c_{1s} &= 2\sin^2\theta \cos\theta \sin\zeta \{\sin(\omega_{\mathrm{eff}}t_p)\sin(\Omega_S\tau) \\
&\quad \times [\cos(\Omega_S\tau)(\cos(\omega_{\mathrm{TN}}T) - 1) \\
&\quad - \sin(\Omega_S\tau)\cos\theta \sin(\omega_{\mathrm{TN}}T)] \\
&\quad + (\cos(\omega_{\mathrm{eff}}t_p) - 1)\cos\zeta \\
&\quad \times [\sin(\Omega_S\tau)\cos(\Omega_S\tau)\cos\theta \sin(\omega_{\mathrm{TN}}T) \\
&\quad - \sin^2(\Omega_S\tau) - \cos^2(\Omega_S\tau)\cos(\omega_{\mathrm{TN}}T)]\},
\end{aligned} \quad [21]$$

and

$$\tan\zeta = \omega_p/\Omega_S \quad [22]$$

$$\omega_{\mathrm{eff}} = [\omega_p^2 + \Omega_S^2]^{1/2}. \quad [23]$$

The factor $\sin\zeta$ describes the suppression of spin packets that are sufficiently off-resonant. For a nonselective preparation $\pi/2$ pulse, $\zeta = \pi/2$ and $\omega_{\mathrm{eff}}t_p = \pi/2$, so that the coefficients in Eq. [21] reduce to

$$\begin{aligned}
c_{2c} &= \sin^2\theta[1 - \sin^2\theta \sin^2(\Omega_S\tau)] \\
c_{2s} &= 0
\end{aligned}$$

TABLE 1
Components of the PEANUT Signal

Signal component	Oscillation frequency	First part of the HTA pulse	Second part of the HTA pulse
Spin-locked echo	0	Locking	Locking
Nutation decay, $t = 0$	ω_{TN}	Driving	Locking
Nutation decay, $t = T$	ω_{TN}	Locking	Driving
Rotary echo, $t = T/2$	$2\omega_{TN}$	Driving	Driving

$$c_{1c} = -2 \cos\theta \sin^2\theta \sin(\Omega_S\tau) \times \{\cos(\Omega_S\tau)\sin(\omega_{TN}T) + \sin(\Omega_S\tau)\cos\theta[1 + \cos(\omega_{TN}T)]\} \quad [24]$$

and

$$c_{1s} = 2 \cos\theta \sin^2\theta \sin(\Omega_S\tau) \times \{\cos(\Omega_S\tau)\,[\cos(\omega_{TN}T) - 1] - \sin(\Omega_S\tau)\cos\theta \sin(\omega_{TN}T)\}.$$

The constant term c_0 (*28*) describes the component of the magnetization that is locked along $\boldsymbol{\omega}_{TN}$ during the two time intervals of the HTA pulse. It does not evolve during time T and refocuses at time τ after the HTA pulse. The underlying coherence transfer pathway is equivalent to a spin-locked echo (*27*). The second and third term in Eq. [20] describe the modulation of the echo amplitude with frequency $2\omega_{TN}$. The doubling of the frequency is a consequence of the MW phase inversion of the HTA pulse at time t. This part of the signal is created by the magnetization components that nutate during the whole HTA pulse and is maximum at time $t = T/2$. The last two terms describe the modulation of the primary echo amplitude with the single nutation frequency ω_{TN}. It is caused by magnetization components that are locked during time t and nutate during time $T - t$, and vice versa. However, since their amplitudes are weighted with $\cos\theta$ (Eq. [21]), only off-resonance spin packets will contribute to this component of the signal. The characteristics of the three types of terms and the effect of the two parts of the HTA pulse on them are summarized in Table 1. Since the singly nutating part is maximum close to $t = 0$ and $t = T$, and dephasing is governed by the off-resonance contribution excited by the preparation pulse, it can in almost all practical cases be separated in time from the doubly nutating part by choosing an appropriate T value. Data acquisition can then be restricted to the central region $T/3 \le t \le 2T/3$, resulting in a considerable saving of measuring time.

For more complex spin systems each transition is characterized by its individual transition moment, affecting the PEANUT signal intensity during excitation and detection. The latter cannot be influenced, since the efficiency of the detection is exclusively determined by the transition moment in the expression for the detection operator. The preparation, however, can be optimized by using a pulse with an *effective* flip angle $\pi/2$ that maximizes the creation of electron coherence. For an $S = \frac{1}{2}$, $I = \frac{1}{2}$ system, for example, the optimum flip angle for the allowed transitions is given by $\beta = (\pi/2)(I_a)^{-1/2}$, which is close to $\pi/2$ (Eq. [17]). For the forbidden transitions the optimum nominal flip angle is $\beta = (\pi/2)(I_f)^{-1/2}$, which is usually much larger than $\pi/2$ (Eq. [18]). Neglecting inhomogeneity and off-resonance effects, the PEANUT signal intensity for optimum preparation is then determined by the transition *moment.* If however a nominal flip angle $\pi/2$ is used, the intensities are determined by the transition *probabilities.* In real experiments, the signal amplitudes are influenced by a number of additional parameters, so that the intensities cannot usually be described by such simple relations.

It should be noted that nuclear spins in the system may manifest themselves in the nutation spectrum as peaks at the nuclear transition frequencies. These undesired features that are caused by the nuclear modulation effect (*22*), and are especially pronounced at the free proton frequency, are considerably weaker in PEANUT than in all the other nutation schemes (*17*). This is because the phase change in the HTA pulse represents an additional forbidden transfer for the nuclear coherence.

An additional advantage of the 2D PEANUT experiment is that proper processing of the collected data allows one to obtain a 1D field-swept EPR spectrum which is closely related to an echo-detected EPR spectrum. The echo-detected spectrum therefore does not have to be recorded separately; it is obtained by calculating the mean values of the PEANUT time traces that correspond approximately to the locked magnetization (signal component c_0 in Eq. [20]). We therefore call the EPR spectrum obtained in this way a *spin-lock projection.*

In the following we illustrate the inner working of the PEANUT sequence by a number of simulations based on the analytical expressions given in Eqs. [20], [21]; only the final integration over the EPR lineshape and the distribution of ω_1 have been computed numerically.

Microwave field strength. Lineshapes along the nutation dimension depend on the ratio between MW field strength and inhomogeneity Γ_{inh} of the EPR line shape. (a) $\omega_1 \ll \Gamma_{inh}$: At MW fields ω_1 small compared to the inhomogeneous linewidth Γ_{inh}, off-resonance effects are very prominent. In the absence of other broadening mechanisms the features of the terms nutating at ω_{TN} and $2\omega_{TN}$ are not fully separated from each other (Fig. 2a, upper left), and the corresponding peaks in the spectrum are asymmetric with long tails at their high-frequency end. In 2D plots these tails that result from off-resonance contributions described by Eq. [7] manifest

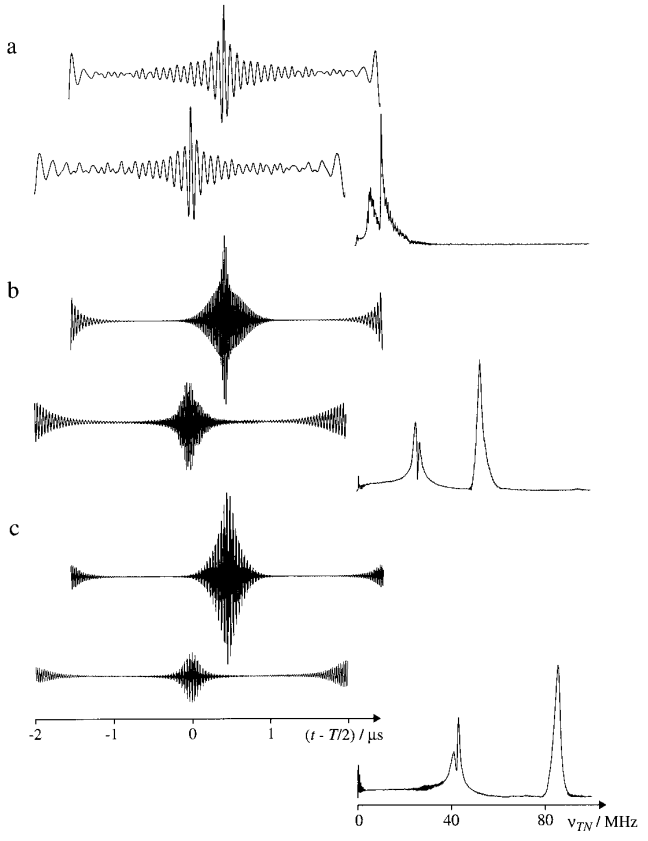

FIG. 2. Effect of the MW field strength ω_1 on the PEANUT nutation pattern, demonstrated on γ-irradiated Herasil quartz. Simulated (upper traces) and experimental (lower traces) time domain data (left) are shown together with the experimental absolute-value spectra (right). (a) $\omega_1/2\pi = 5.68$ MHz $< \Gamma_{inh}/2\pi$, (b) $\omega_1/2\pi = 25.21$ MHz $\approx \Gamma_{inh}/2\pi$, (c) $\omega_1/2\pi = 43.00$ MHz $> \Gamma_{inh}/2\pi$. Parameters: length of preparation pulse $t_p = 10$ ns, length of HTA pulse $T = 4$ μs, $\tau = 700$ ns.

themselves as ridges, which can only be observed in specially chosen samples with narrow lines (see below). (b) $\omega_1 \approx \Gamma_{inh}$: For this situation the singly and doubly nutating features are nicely separated in the time (Fig. 2b, upper left), and the frequency domain and the high-field tails are less pronounced. (c) $\omega_1 > \Gamma_{inh}$: If ω_1 exceeds Γ_{inh} the two oscillation patterns are fully separated (Fig. 2c, upper left) and the peak at $2\omega_{TN}$ is virtually symmetric, since for all spin packets involved in the experiment, $\omega_{TN} \approx \omega_1$. (d) $\omega_1 \gg \Gamma_{inh}$: In this case off-resonance effects can be neglected so that the singly nutating features and the coefficient c_{2s} of the doubly nutating frequency vanish ($\theta \approx \pi/2$, see Eq. [21]). Note that in all the simulations and corresponding experimental verifications shown in Figs. 2–4, for illustrative purposes the entire time domain signals, containing both the ω_{TN} and $2\omega_{TN}$ frequency, are Fourier transformed. In a real experimental application the frequencies ω_{TN} can easily be eliminated by considering only the center part of the time domain signal (see above).

Suppression effects. All the coefficients in Eqs. [21] and [24] depend on time τ and the resonance offset Ω_S, so that spin packets with particular values of $(\Omega_S\tau)$ will not contribute to the signal. After integration over Ω_S this results in a hole pattern imposed on the high-frequency tails of the peaks which is caused by the square root relationship of the nutation frequency (Eq. [7]). The effect is shown in Figs. 3a and 3b (left) for $\tau = 300$ and 700 ns. With increasing τ values the amplitude of the modulation pattern gets shallower and the frequency increases. The suppression effects can only be observed in systems with very sharply defined nutation frequencies. In most practical applications it is of no relevance.

Selective preparation. The selectivity of the PEANUT experiment can be controlled by the length of the preparation pulse. A preparation pulse of duration t_p excites only spins within a frequency window of about $2\pi/t_p$. Correspondingly, a longer preparation pulse yields a smaller linewidth in the nutation spectrum, as long as offset effects contribute to the linewidth ($\omega_1 \leq \Gamma_{inh}$). This is demonstrated in Figs. 4a and 4b (left) for two preparation pulses of length 10 and 300 ns with a nominal flip angle $\pi/2$.

EXPERIMENTAL

Experiments on γ-irradiated Herasil quartz, a simple $S = \frac{1}{2}$ system, were carried out at a temperature of 180 K and an MW frequency of 9.041 GHz on a homebuilt pulse X-band EPR spectrometer (*30*) equipped with a probehead with a dielectric ring resonator (*1*). With this spectrometer, higher pulse power (corresponding MW field strength: $\omega_1/2\pi \approx 120$ MHz for $g = 2$) can be achieved than with the Bruker ESP 380E spectrometer. The intrinsic inhomogeneous width of the spectrum of 0.2 mT was increased to about 1 mT by

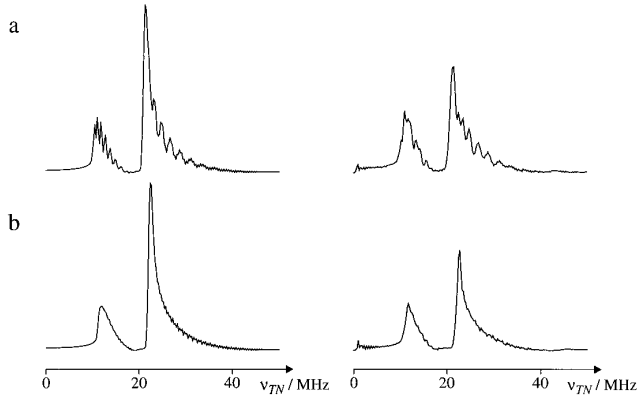

FIG. 3. Demonstration of the suppression effect in PEANUT experiments performed on γ-irradiated Herasil quartz. Simulated (left) and experimental (right) nutation spectra are shown for two different τ values. (a) $\tau = 300$ ns, (b) $\tau = 700$ ns. Parameters: length of preparation pulse $t_p = 10$ ns, length of HTA pulse $T = 4$ μs.

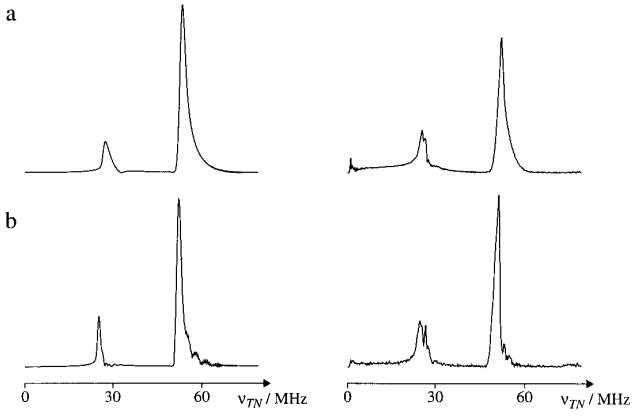

FIG. 4. Influence of the selectivity of the preparation $\pi/2$ pulse on the linewidth in PEANUT experiments. (Left) Simulations, (right) experiments performed on γ-irradiated Herasil quartz. Length of the preparation pulse (a) t_p = 10 ns, (b) t_p = 300 ns. Parameters: length of HTA pulse T = 4 μs, τ = 700 ns.

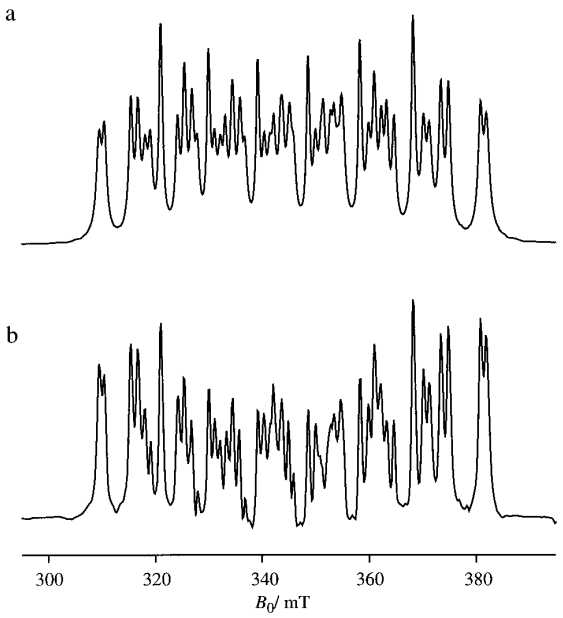

FIG. 6. Single crystal EPR spectra of Mn^{2+}-doped $CaCO_3$. (a) Two-pulse echo-detected EPR spectrum, (b) spin-lock projection EPR spectrum.

applying a static magnetic field gradient along $\mathbf{B}_0$. If not specially mentioned the entire time domain signals have been Fourier transformed and absolute-value spectra have been calculated. No apodization or zero filling has been used.

PEANUT experiments on Mn^{2+}-doped powders and single crystals were performed on a Bruker ESP-380E pulse X-band EPR spectrometer equipped with a dielectric resonator (Bruker EN 4118) and a helium gas flow cryostat from Oxford. The pulse channels were calibrated by maximizing the echo amplitude in a two-pulse spin echo experiment. A detection window of 24 ns centered at time τ after the HTA pulse was used. All time domain signals were recorded using quadrature detection. The data were then apodized with a $\sin^2$ window, zero-filled to 256 points, and Fourier transformed along the nutation dimension. In these figures again absolute-value spectra are shown.

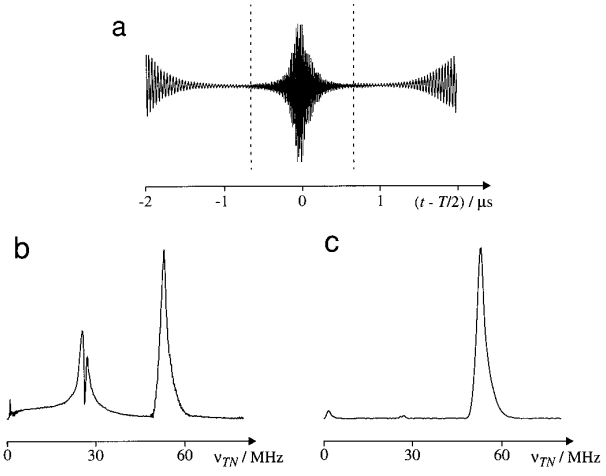

FIG. 5. Influence of the time domain window used for Fourier transformation on the spectrum, demonstrated on γ-irradiated Herasil quartz, $\omega_1/2\pi$ = 25.21 MHz. (a) Time domain trace, dashed lines mark time interval used in (c). (b) Absolute-value spectrum obtained with the full data set. (c) Absolute-value spectrum for $-0.66 \leq t - \frac{T}{2} < 0.66$ μs.

For spin-lock projection EPR a Mn^{2+}-doped $CaCO_3$ single crystal with two inequivalent Mn^{2+} sites with different hyperfine parameters has been used. Mn^{2+}-doped CaO powder was equilibrated with water and then dried at 200°C under high vacuum for several hours to define a reproducible water content. Mn^{2+}-doped $La_2Mg_3(NO_3)_{12} \cdot 24H_2O$ single crystals were grown from aqueous solution. Spectra of the $[Mn(H_2O)_6]^{2+}$ centers in the $La_2Mg_3(NO_3)_{12} \cdot 24H_2O$ single crystal at an arbitrary orientation were measured at a temperature of 15 K and an MW frequency of 9.723 GHz. For the CW EPR spectrum, an MW power of 63 μW and a modulation amplitude of 50 μT (peak-to-peak) were employed. The phase cycle $[0]-[\pi]$ for the MW $\pi/2$ pulse of duration t_p = 64 ns has been used. Other parameters are τ = 248 ns, T = 2408 ns, starting value t_0 = 800 ns, time increment Δt = 8 ns, and field increment ΔB_0 = 50 μT. The size of the data matrix was given by 100 points in the nutation dimension (symmetric to $T/2$) and 2801 points in the B_0-field dimension. A cubic function was used for baseline correction in the time domain. Numerical computations have been performed using the C++ library GAMMA (*31*).

RESULTS AND DISCUSSIONS

In this experimental section we verify some of the theoretically predicted features of the PEANUT approach, show a

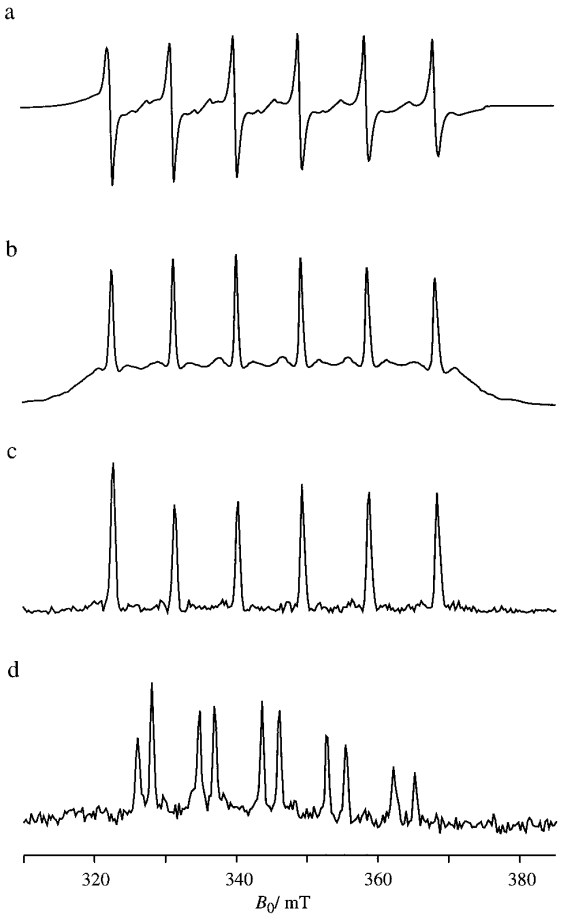

FIG. 7. EPR spectra of Mn^{2+}-doped CaO recorded at 15 K. (a) Continuous wave EPR spectrum. (b) Two-pulse echo-detected EPR spectrum with six strong and narrow $|\frac{1}{2}, m_1\rangle \leftrightarrow |-\frac{1}{2}, m_I\rangle$ transitions and weak and broad $|\pm\frac{3}{2}, m_I\rangle \leftrightarrow |\pm\frac{1}{2}, m_I\rangle$ transitions. (c) Cross-section of the 2D PEANUT spectrum at 25 MHz showing the six $|\frac{1}{2}, m_I\rangle \leftrightarrow |-\frac{1}{2}, m_I\rangle$ transitions. (d) Cross-section of the 2D PEANUT spectrum at 4 MHz showing the 10 forbidden transitions. $|\frac{1}{2}, m_I\rangle \leftrightarrow |-\frac{1}{2}, m_I \pm 1\rangle$.

spin-lock projection EPR spectrum, and present two examples of applications, one of a disordered and one of an ordered system.

Verification of Spectral Features

For the experimental verifications we made use of a γ-irradiated Herasil quartz sample with an artificially increased inhomogeneous linewidth. The experimental data in Fig. 2 (lower time domain traces and corresponding absolute-value spectra) demonstrate the influence of ω_1 on the time domain signals and the corresponding spectra; simulations and experiments are in good agreement. The lineshape of the peak at $2\omega_{TN}$ becomes virtually symmetric at high nutation frequencies (Fig. 2c, right) as predicted by theory. The intensity of the $2\omega_{TN}$ signal is however considerably weaker at high ω_1 than in the corresponding simulation. This is because already small misadjustments of phase and amplitude between the two time periods of the subdivided HTA pulse lead to incomplete refocusing of the nutation echo. The influence of a properly chosen reduced time domain data trace on the spectrum is shown in Fig. 5 for the case $\omega_1 \approx \Gamma_{inh}$. The full data trace (Fig. 5b) and only 1/3 of the time domain data centered around $t - T/2 = 0$ (Fig. 5c) are considered. In the case of the reduced data set, the peak at ω_{TN} is found to be virtually absent. The narrow hole in the peaks at ω_{TN} in Figs. 2 and 5 is traced back to an artifact introduced by the data handling.

The modulation patterns imposed on the high-frequency tails of the ω_{TN} and $2\omega_{TN}$ peaks which were predicted from the τ-dependence of the coefficients in Eqs. [21] could also very nicely be verified. Figures 3a and 3b (right) show the two experimental PEANUT spectra for $\tau = 300$ ns (a) and 700 ns (b). Apart from the above-mentioned different intensity ratios $I(\omega_{TN})/I(2\omega_{TN})$, the spectra show the same features as found in the corresponding simulations (Figs. 3a, 3b, left).

Finally, also the dependence of the linewidth on the length t_p of the preparation pulse could be verified. Figures 4a and 4b (right) show experimental nutation spectra recorded with $t_p = 10$ ns (a) and 300 ns (b). The linewidth is found to be considerably narrower for longer preparation pulses, in agreement with theory.

Spin-Lock Projection EPR Spectrum

The spin-lock projection approach is exemplified on a Mn^{2+}-doped $CaCO_3$ single crystal. In Fig. 6 the two-pulse echo-detected EPR spectrum (a) is compared with the EPR spectrum obtained by computing the spin-lock projection (b) from the 2D PEANUT time domain data. The same peak positions are found in both spectra.

Examples of Application

(1) Separation of allowed and forbidden transitions in a disordered system. Mn^{2+}-doped CaO is used to demon-

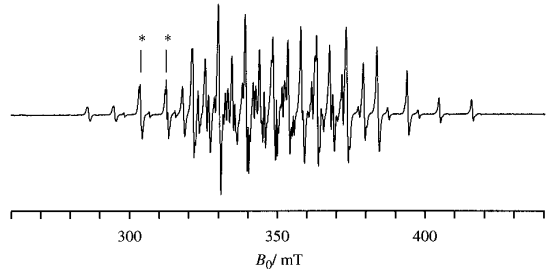

FIG. 8. Continuous wave EPR spectrum of $[Mn(H_2O)_6]^{2+}$ centers in a single crystal of Mn^{2+}-doped $La_2Mg_3(NO_3)_{12} \cdot 24H_2O$ at arbitrary orientation, recorded at 15 K. The spectra of two different types of hexaquo complexes are superimposed. The asterisks designate two lines where signals due to both centers nearly coincide and are unresolved.

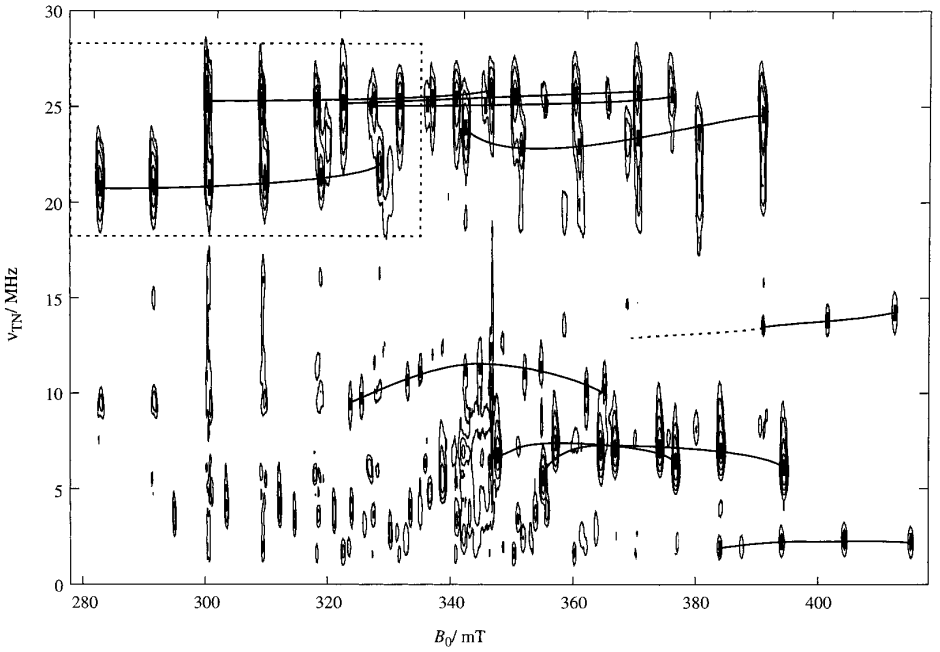

FIG. 9. Contour plot (logarithmic levels) of a 2D PEANUT spectrum of $[Mn(H_2O)_6]^{2+}$ centers in a single crystal of Mn^{2+}-doped $La_2Mg_3(NO_3)_{12}\cdot 24H_2O$ at the same orientation as in Fig. 9. Groups of peaks that differ only in the magnetic quantum number of the manganese nucleus are connected by bold lines.

strate the potential of PEANUT for the measurement of weak forbidden lines. In this $S = \frac{5}{2}$, $I = \frac{5}{2}$ spin system, 30 allowed EPR transitions, namely $|\frac{1}{2}, m_I\rangle \leftrightarrow |-\frac{1}{2}, m_I\rangle$, $|\pm\frac{3}{2}, m_I\rangle \leftrightarrow |\pm\frac{1}{2}, m_I\rangle$, and $|\pm\frac{5}{2}, m_I\rangle \leftrightarrow |\pm\frac{3}{2}, m_I\rangle$ are expected. In the CW and pulse field-swept EPR powder spectra shown in Figs. 7a, 7b, the six $|\frac{1}{2}, m_I\rangle \leftrightarrow |-\frac{1}{2}, m_I\rangle$ transitions are observed as sharp peaks (almost isotropic **g** and Mn^{2+}-hyperfine matrices). The $|\pm\frac{3}{2}, m_I\rangle \leftrightarrow |\pm\frac{1}{2}, m_I\rangle$ transitions manifest in the CW EPR spectrum as broad features. The $|\pm\frac{5}{2}, m_I\rangle \leftrightarrow |\pm\frac{3}{2}, m_I\rangle$ transitions are broadened beyond observation because of their strong orientation dependence. In addition to the allowed transition, 10 narrow forbidden transitions $|\frac{1}{2}, m_I\rangle \leftrightarrow |-\frac{1}{2}, m_I \pm 1\rangle$ are expected. Part of these forbidden transitions can only be observed in the CW EPR spectrum where they overlap with the $|\pm\frac{3}{2}, m_I\rangle \leftrightarrow |\pm\frac{1}{2}, m_I\rangle$ transitions (Fig. 7a).

In the 2D PEANUT plot, ω_{TN} versus B_0 field, recorded with $\omega_1/2\pi \approx 5$ MHz the allowed transitions are observed in the nutation frequency region 20 MHz $< 2\omega_{TN}/2\pi <$ 30 MHz, with the frequencies of the six $|\frac{1}{2}, m_I\rangle \leftrightarrow |-\frac{1}{2}, m_I\rangle$ peaks at the high frequency end of the spectrum ($2\omega_{TN} \approx 6\,\omega_1$, Eq. [19]). The cross-section of these features is shown in Fig. 7c. The 10 forbidden transitions nutate at a frequency $2\omega_{TN}/2\pi \approx 4$ MHz, which is considerably lower than that of the allowed transitions. The corresponding cross-section shown in Fig. 7d contains only the forbidden transitions. Since the linewidth of the allowed and forbidden transitions in the ω_{TN} dimension is about 3 MHz (FWHH), their spectra are fully separated from each other. The PEANUT peaks are found to be significantly narrower than the corresponding peaks obtained from the echo amplitude modulation in a $\pi/2-\tau-HTA(T)-\tau-$echo spin-locked sequence where an HTA pulse without phase change is used, and also narrower than the peaks observed in the echo-detected and FID-detected nutation experiments.

(2) Separation of peaks belonging to different sites and magnetic quantum numbers in an ordered system. The improvements in resolution and the simplification of assignment problems are exemplified by measurements on a single crystal of Mn^{2+}-doped $La_2Mg_3(NO_3)_{12}\cdot 24H_2O$. This sample features two types of $[Mn(H_2O)_6]^{2+}$ centers: Type I with trigonal and inversion symmetry and type II with only trigonal symmetry (*32*, *33*). For both types, second-order effects due to manganese hyperfine coupling and the zero-field splitting are significant so that the splittings within the hyperfine multiplets (i.e., six transitions that differ only in the magnetic quantum number of the manganese nucleus) are not equal. In addition one also observes forbidden transitions. As a result, even the single crystal EPR spectrum is not properly resolved and the peaks are difficult to assign (Fig. 8). The introduction of the nutation frequency as a second dimension improves resolution drastically, as is demonstrated by the contour plot in Fig. 9 (logarithmic levels). A number of hyperfine multiplets can now easily be recognized. Note that because of the large intensity variations in the PEANUT spectrum, the information cannot be fully exploited with only one set of contour levels. For instance,

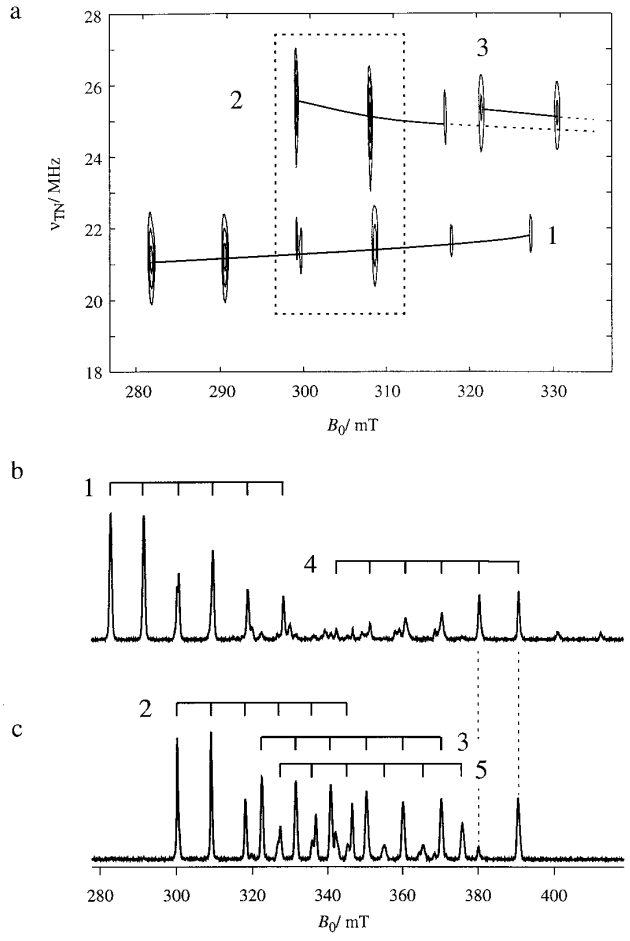

FIG. 10. Details of the 2D PEANUT spectrum of $[Mn(H_2O)_6]^{2+}$ centers in a single crystal of Mn^{2+}-doped $La_2Mg_3(NO_3)_{12}\cdot 24H_2O$ shown in Fig. 9. Groups of peaks that differ only in the magnetic quantum number of the manganese nucleus are labeled by numbers 1 ··· 5. (a) Dashed box in Fig. 9 with higher contour levels (see also asterisks in Fig. 8). (b) Cross-section of the PEANUT spectrum at 21 MHz. (c) Cross-section of the PEANUT spectrum at 25.6 MHz.

the good resolution of the two pairs of overlapped EPR lines labeled by asterisks in Fig. 8 can only be appreciated in the detail contour plot in Fig. 10a (dashed box in Fig. 9), where the lowest levels are not shown. The method that turned out to be the most successful for analyzing such 2D PEANUT spectra is to use cross-sections with a fixed nutation frequency as is shown in Figs. 10b and 10c. These cross-sections can be considered as *nutation frequency selective EPR spectra*. Comparison with Fig. 8 reveals that such spectra are often much better resolved than a CW EPR spectrum. The two traces shown in Figs. 10b and 10c allow one to unequivocally assign five hyperfine multiplets corresponding to allowed transitions. Note also that it is not necessary to assign each peak in the whole PEANUT spectrum in order to obtain the Hamiltonian parameters, since they are highly overdetermined by the frequencies and transition moments of all EPR transitions. This redundancy allows one to discard regions of the spectrum where even in the 2D PEANUT experiment the features are not fully resolved. Such a region appears for the Mn^{2+}-doped $La_2Mg_3(NO_3)_{12}\cdot 24H_2O$ single crystal between 340 and 350 mT in the nutation frequency range from 3 to 10 MHz (see Fig. 9).

CONCLUSION

The 2D PEANUT experiment introduced in this work allows a field-swept EPR spectrum to be spread into a second dimension, according to the transition moments of the individual EPR lines. The approach is instrumentally less demanding than other methods for disentangling EPR spectra and can easily be implemented on any pulse EPR spectrometer. In disordered systems PEANUT may also help to find the proper field position for experiments like ESEEM or pulse ENDOR. The applicability of very high nutation fields and relatively narrow spectral features make PEANUT superior to all the other nutation methods. This we found by comparing the different types of nutation experiments mentioned in the introduction, carried out at one of the central transitions of the powder spectrum of Mn^{2+}-doped CaO (*17*). Moreover, the undesired feature at the free proton frequency caused by the nuclear modulation effect of protons in the vicinity of the unpaired electron is found to be much weaker in the PEANUT experiment than in the other approaches.

ACKNOWLEDGMENTS

This research has been supported by the Swiss National Science Foundation. G.J. thanks the Stiftung Stipendium-Fonds des Verbandes der Chemischen Industrie (Germany) for a Kekulé grant. S.S. thanks the Technische Universität Graz (Austria) for financial support. We are grateful to Professor Daniella Goldfarb for helpful discussions. The manuscript has been processed by Mrs. I. Müller.

REFERENCES

1. G. Sierra and A. Schweiger, *Rev. Sci. Instrum.* **68,** 1316 (1997).
2. G. Sierra, A. Schweiger, and R. R. Ernst, *Chem. Phys. Lett.* **184,** 363 (1991).
3. M. Willer and A. Schweiger, *Chem. Phys. Lett.* **230,** 67 (1994).
4. I. I. Rabi, *Phys. Rev.* **51,** 652 (1937).
5. C. Torrey, *Phys. Rev.* **76,** 1059 (1949).
6. B. C. Gerstein, *in* ''Encyclopedia of Nuclear Magnetic Resonance'' (D. M. Grant and R. K. Harris, Eds.), Vol. 5, p. 3360, Wiley, New York (1996).
7. C. Gemperle, A. Schweiger, and R. R. Ernst, *Chem. Phys. Lett.* **145,** 1 (1988).
8. D. Stehlik, C. H. Bock, and M. C. Thurnauer, *in* ''Advanced EPR'' (A. J. Hoff, Ed.), p. 371, Elsevier, Amsterdam (1989).
9. V. Konskov, D. J. Sloop, S.-B. Liu, and T.-S. Lin, *J. Magn. Reson. A* **117,** 9 (1995).

10. R. Hanaishi, Y. Ohba, S. Yamanchi, and M. Iwaizumi, *Bull. Chem. Soc. Jpn.* **69,** 1533 (1996).

11. R. Bittl and G. Kothe, *Chem. Phys. Lett.* **177,** 547 (1991).

12. R. Hanaishi, Y. Ohba, K. Akiyama, S. Yamanchi, and M. Iwaizumi, *J. Magn. Reson. A* **116,** 196 (1995).

13. M. K. Bowman, *in* ''Modern Pulsed and Continuous-Wave Electron Spin Resonance'' (L. Kevan and M. K. Bowman, Eds.), p. 1, Wiley, New York (1990).

14. J. Isoya, H. Kanda, J. R. Norris, J. Tang, and M. K. Bowman, *Phys. Rev. B* **41,** 3905 (1990).

15. A. V. Astashkin and A. Schweiger, *Chem. Phys. Lett.* **174,** 595 (1990).

16. T. Takui, K. Sato, D. Shiomi, K. Itoh, T. Kaneko, E. Tschchida, and H. Nishide, *Mol. Cryst. Liq. Cryst.* **279,** 155 (1996).

17. S. Stoll, Diploma thesis, ETH Zürich (1996).

18. I. Solomon, *Phys. Rev. Lett.* **2,** 301 (1959).

19. A. Schenzle, N. C. Wong, and R. G. Brewer, *Phys. Rev. A* **21,** 887 (1980).

20. M. Willer and A. Schweiger, *Chem. Phys. Lett.* **264,** 1 (1997).

21. A. R. Edmonds, ''Angular Momentum in Quantum Mechanics,'' Princeton Univ. Press, Princeton, NJ (1957).

22. A. Schweiger, *in* ''Modern Pulsed and Continuous-Wave Electron Spin Resonance'' (L. Kevan and M. K. Bowman, Eds.), p. 43, Wiley, New York (1990).

23. A. Samoson and E. Lippmaa, *Phys. Rev. B* **28,** 6567 (1983).

24. P. P. Man, *J. Magn. Reson.* **67,** 78 (1986).

25. A. P. M. Kentgens, J. J. M. Lemmens, F. M. M. Geurts, and W. S. Veeman, *J. Magn. Reson.* **71,** 62 (1987).

26. A. Samoson and E. Lippmaa, *Chem. Phys. Lett.* **100,** 205 (1983).

27. A. Ponti and A. Schweiger, *Appl. Magn. Reson.* **7,** 363 (1994).

28. M. Willer, Thesis, ETH Zürich, 1997.

29. S. Boentges, ''Computer Program: SOME (Spin Operator Manipulation Environment)'' (1992).

30. Th. Wacker, Ph.D. thesis, ETH Zürich, No. 9913 (1992).

31. S. A. Smith, T. O. Levante, B. H. Meier, and R. R. Ernst, *J. Magn. Reson.* **68,** 442 (1994).

32. D. van Ormondt, R. De Beer, M. Brouha, and F. De Groot, *Z. Naturforsch. A* **24,** 1746 (1969).

33. A. Zalkin, J. D. Forrester, and D. T. Templeton, *J. Chem. Phys.* **39,** 2881 (1963).